PHYSICAL REVIEW A **109**, L061501 (2024)

**Letter** **Editors' Suggestion**

# Mesoscopic non-Hermitian skin effect

Alexander Poddubny,[1,*] Janet Zhong,[2,†] and Shanhui Fan[2]

[1]*Department of Physics of Complex Systems, Weizmann Institute of Science, Rehovot 7610001, Israel*
[2]*Department of Applied Physics, Stanford University, Stanford, California 94305, USA*

(Received 14 October 2023; revised 12 May 2024; accepted 14 May 2024; published 3 June 2024)

We discuss a generalization of the non-Hermitian skin effect to finite-size photonic structures with neither gain nor loss in the bulk and a purely real energy spectrum under periodic boundary conditions (PBCs). We show that despite being Hermitian in the bulk, such systems can still have significant portions of eigenmodes concentrated at the edges and that this edge concentration can be linked to the nontrivial point-gap topology of the size-dependent regularized PBC spectrum, accounting for the radiative losses due to photon emission through the edges. We focus on a particular example of an array of atoms chirally coupled to the waveguide, but our results are also applicable to other systems with losses through the edges.

DOI: 10.1103/PhysRevA.109.L061501

*Introduction.* The non-Hermitian skin effect (NHSE) is manifested by the concentration of the eigenmodes at the edge of a finite structure under open boundary conditions (OBCs), that is related to the nontrivial point-gap topology under periodic BCs (PBCs) [1–7]. The energy spectrum drastically changes under the OBCs, contrary to the usual Hermitian systems. A paradigmatic example is the Hatano-Nelson model of a one-dimensional lattice with different left- and right-tunneling coupling constants $t_1 \neq t_2$ [8] [see Fig. 1(a)]. Its PBC spectrum has a loop in the complex plane with a nonzero area, that under OBC collapses into a line corresponding to edge-concentrated eigenmodes.

Particular realizations of NHSE can be very different, such as tight-binding lattices, photonic crystals [9,10], continuous media [11], and even lattices in synthetic dimensions [12]. One of the simplest inherently non-Hermitian setups is an optical cavity. Indeed, if the cavity has a finite size and the permittivity of its material is finite, there is always a nonzero possibility of the photon emission in the far field [13]. This translates into the finite quality factor and non-Hermitian effective Hamiltonian $H$ for the cavity eigenmodes. Here, however, we would like to stress a difference between the non-Hermiticity arising due to the emission into the far field and the non-Hermiticity because of the internal loss or gain (as in the Hatano-Nelson case). In the former case the structure has no loss or gain in the bulk. It becomes effectively Hermitian in the limit of infinite size, and its energy spectrum is real valued. On the other hand, as long as the structure is finite, it is still non-Hermitian. We find that despite the absence of bulk gain or loss, periodic chiral Hermitian photonic structures can still exhibit an analog of the NHSE, but a very special one: The imaginary part of the eigenfrequencies and the localization length will depend on the structure size. We term this a mesoscopic NHSE.

As a particular example we consider the mesoscopic NHSE in a chiral waveguide quantum electrodynamics (WQED) setup, that is, an array of natural or artificial atoms, chirally coupled to the waveguide [14–18]. An infinite periodic array has a purely real PBC spectrum and neither loss nor gain in the bulk [see Figs. 1(b) and 1(d)]. When a number of emitters is finite, an array acquires radiative losses due to the photon escape into the waveguide, so the OBC spectrum becomes complex. These OBC eigenmodes can also concentrate at one edge when the structure is chiral. We aim to link this concentration to the nontrivial point-gap topology of dispersion law $\omega(K)$ for complex wave vectors $K$. To this end, we propose a regularization of the $\omega(K)$ dependence for a finite structure. The real-valued PBC spectrum is dramatically modified by this regularization. It becomes complex and encircles the OBC spectrum [see the horseshoe contours in Fig. 1(d)], just as in the usual NHSE case of Fig. 1(c).

While such arrays are known to have eigenmodes concentrated at the edges [19–24], we believe that the size-dependent connection to the NHSE is not yet fully understood. In particular, while Ref. [20], with one of us as a coauthor, analyzed the eigenmodes in great detail, this work has not mentioned any topological spectral features. References [23,24] considered a very similar setup for magnons that, however, had a nonzero internal nonradiative loss. References [21,22] did discuss NHSE in substantially different chiral atomic systems, where the primary loss mechanism was not at the edges. Thus, despite significant progress, the general consequences of having only radiative loss at the edge for NHSE and for non-Hermitian physics apparently remain unclear.

*Model.* We consider single-excited eigenstates in an array of $N$ periodically spaced emitters described by the effective non-Hermitian Hamiltonian [19] $H = \sum_{m,n=1}^{N} H_{m,n}\sigma_n^\dagger \sigma_m$ with $\sigma_m^\dagger$ being the raising operators and

$$H_{m,n} = \omega_0 \delta_{m,n} - i \begin{cases} \gamma_{\rightarrow} e^{i\varphi|m-n|}, & m > n, \\ \frac{\gamma_{\rightarrow}+\gamma_{\leftarrow}}{2}, & m = n, \\ \gamma_{\leftarrow} e^{i\varphi|m-n|}, & m < n, \end{cases} \tag{1}$$

where $\gamma_{\rightarrow} = 2\gamma_{1D}/(1+\xi)$ and $\gamma_{\leftarrow} = 2\gamma_{1D}\xi/(1+\xi)$ are the spontaneous emission rates into the waveguide in the forward

---

[*] poddubny@weizmann.ac.il
[†] janetzh@stanford.edu

©2024 American Physical Society

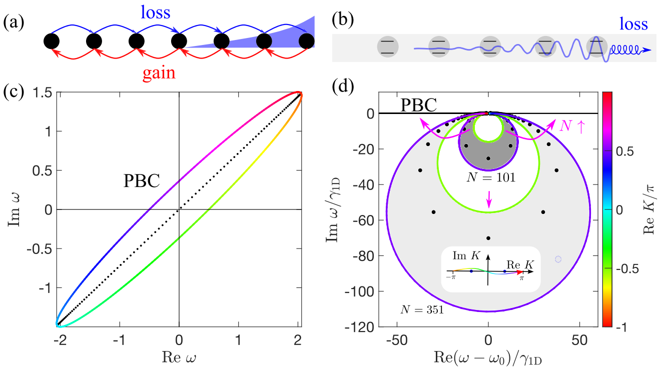

FIG. 1. (a), (b) Schematics of (a) the Hatano-Nelson model with spatially distributed gain and loss and (b) a chiral waveguide-QED model with radiative loss on the edges. (c), (d) Spectra under periodic boundary conditions (PBCs, colored lines) and open boundary conditions (OBCs, black dots) in these models. The Hatano-Nelson model corresponded to $t_1 = 1 + 0.5\mathrm{i}$, $t_2 = 1 + \mathrm{i}$, and $N = 102$ sites. Two horseshoe-shaped lines in (d) are regularized PBCs for $N = 101$ and $N = 351$. Magenta arrows indicate how the spectrum transforms when $N$ grows. The inset illustrates the complex $K$ contour used for regularized PBCs avoiding the two poles at $K = \pm\varphi$ (blue dots). Calculated for $\xi = 1/2$ and $\varphi = \pi/2$.

and backward directions. The phase $\varphi = \omega_0 d/c$ is the phase gained by light between the two emitters. We use the Markovian approximation, valid for $\gamma_{1D} \ll \omega$, so that the frequency dependence of $\varphi$ is ignored. Notably, the Hamiltonian Eq. (1) features long-range photon-mediated coupling between distant emitters. The parameter $\xi$ is the ratio of emission rates in the forward and backward directions. Under the PBC, the Hamiltonian matrix $H_{mn}$ has the eigenstates $\psi_m = e^{iKm}$ with the eigenenergies

$$\omega(K) = \omega_0 + \gamma_{1D}\frac{\sin\varphi + \chi\sin K}{\cos K - \cos\varphi}, \tag{2}$$

where

$$\chi = \frac{1-\xi}{1+\xi}.$$

Importantly, the energy spectrum Eq. (2) is purely real. It features a singularity near the light line, $K = \varphi$, and a polaritonic band gap near the resonance frequency $\omega_0$. We can also rewrite the dispersion law in the effective-medium approximation, assuming $\varphi \ll 1$, $K \ll 1$, that leads to $K^2 = \varphi^2\varepsilon(\omega, K)$ where $\varepsilon_{\mathrm{eff}}(\omega, K) = 1 + (2\gamma_{1D}/\varphi)(1 + \chi K)/(\omega_0 - \omega)$ is the resonant permittivity. The breakdown of the time-reversal symmetry for $\chi \neq 0$ is manifested by the linear-in-$K$ term in $\varepsilon_{\mathrm{eff}}$.

The OBC spectrum can be obtained either by diagonalizing Eq. (1) or by solving the Eq. [20,25]

$$r_{\hookrightarrow} r_{\hookleftarrow} e^{i(K_+ - K_-)(N-1)} = 1, \quad r_{\substack{\hookrightarrow\\ \hookleftarrow}} = -\frac{e^{\pm iK_\pm} - e^{i\varphi}}{e^{\pm iK_\mp} - e^{i\varphi}}, \tag{3}$$

where $r_{\hookrightarrow/\hookleftarrow}(\omega)$ are the reflection coefficients of the polaritons from the inside of the structure and $K_\pm(\omega)$ are the solutions of Eq. (2). Equation (3) describes standing waves in the cavity made of resonant chiral material with the (effective) permittivity $\varepsilon_{\mathrm{eff}}$. The chiral WQED is related to the nonreciprocal waveguide system [26], that has attracted a lot of interest [27–30].

*Mescoscopic NHSE.* Figure 2 presents the eigenstates and the OBC spectra calculated for the finite arrays with $N = 101$ emitters for two different asymmetry parameters $\xi = 0.5$ [Figs. 2(a) and 2(b)] and $\xi = 0.05$ [Figs. 2(c) and 2(d)]. In both cases, the structures feature superradiant modes with a much larger decay rate than the single atom decay rate $\gamma_{1D}$ [20].

The eigenmodes in Figs. 2(a) and 2(c) are ordered by the decreasing radiative decay rate. It is clear that they become pinned to the edges for a higher decay rate. In the more chiral case [Fig. 2(c)], a large fraction of eigenmodes is concentrated at just one edge, which looks like the hallmark of the NHSE. The eigenmode spatial profile is given by an exact analytical Eq. [20]

$$\begin{aligned}\psi_m &\propto e^{iK_+(m-N)} + r_{\hookleftarrow} e^{iK_-(m-N)} \\ &\propto e^{iK_+(m-1)} r_{\hookrightarrow} + e^{iK_-(m-1)},\end{aligned} \tag{4}$$

where $z_\pm = \exp[iK_\pm(\omega)]$ are found by inverting Eq. (2) at the mode eigenfrequency $\omega$ and can be approximated by

$$K_\pm \approx \pm\frac{\pi}{2} + (\chi \mp 1)\frac{\gamma_{1D}}{\omega - \omega_0}. \tag{5}$$

Equation (5) shows that modes with larger radiative losses are also the more localized modes, that is, with a larger $|\operatorname{Im} K_\pm|$. The difference between $\operatorname{Im} K_+$ and $\operatorname{Im} K_-$ also increases with chirality. This results in the concentration of the brightest eigenmodes (that is, with the largest radiative decay rate $-\operatorname{Im}\omega_\nu$) at one particular edge (see also Supplemental Fig. S3 [31] for more detail). For $|\omega - \omega_0| \gg \gamma_{1D}$ and $\varphi = \pi/2$ we can obtain from Eq. (3) an approximate OBC spectrum

$$\omega_\nu^\pm - \omega_0 = -\frac{iN\gamma_{1D}}{W_\nu(\pm 2N/\sqrt{1-\chi^2})}, \quad \nu = 0, \pm 1, \ldots, \tag{6}$$

of the most superradiant modes, which is shown by open circles in Figs. 2(b) and 2(d) and well describes the numerical results. Here, $W_\nu(z)$ is the Lambert function, satisfying the equation $W_\nu e^{W_\nu} = z$.

While the eigenmodes in Fig. 2(d) are concentrated at one edge, there are two important distinctions from the conventional NHSE case. First, only one of the eigenvalues $z_\pm \equiv e^{iK_\pm}$ in Eq. (4) is larger than unity by the absolute value, and the other one is smaller than unity. From now on, we will label the larger eigenvalue $z_2$ and the smaller one $z_1$. Hence, the eigenfunction $\psi_m$ in Eq. (4) contains two exponents, localized at the left and right edges of the structure. It is still preferentially localized at just one edge, because the amplitudes of these two exponents are different for nonzero chirality. This is quite distinct from the conventional NHSE such as in the Hatano-Nelson model, where $|z_1| = |z_2|$ and either $|z_{1,2}| > 1$ or $|z_{2,1}| < 1$, with certain special exceptions for the case of local perturbations or modification of boundary conditions [32–35]. The conventional complex tight-binding model with open boundary conditions will have $|z_1| = |z_2|$ except at the edge states as per the generalized Brillouin zone condition [4]. A second difference is more subtle. Not only do we have $|z_2| > 1$ and $|z_1| < 1$, but the values of $z_2$ and $z_1$ also depend

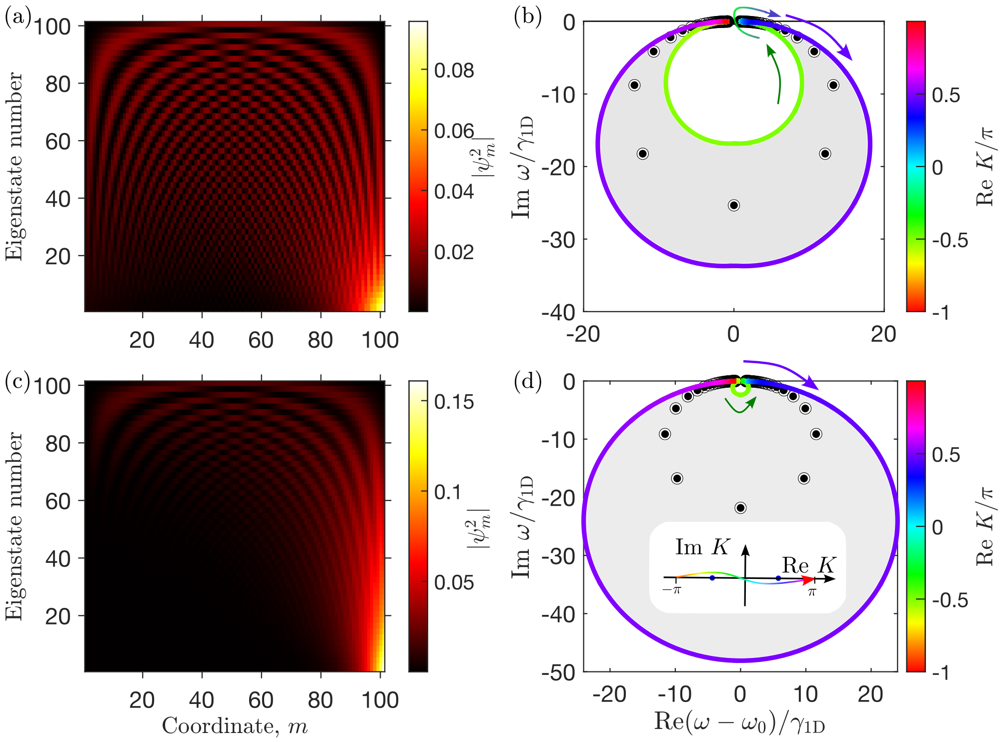

FIG. 2. (a), (c) Eigenmodes and (b), (d) energy spectrum of the structure with $N = 101$ emitters and (a), (b) $\xi = 0.5$ and (c), (d) $\xi = 0.05$. Solid circles correspond to the numerical solution, and open circles are calculated according to Eq. (6). The eigenmodes in (a) and (c) are presented in descending order of the radiative decay rate $-\operatorname{Im}\omega$. The PBC spectrum is shown by colored lines in (c) and (d). The inset in (d) schematically illustrates the complex $K$ contour used for the PBC calculation. Calculated for $\varphi = \pi/2$.

on $N$. It follows from Eqs. (5) and (6) that $-\operatorname{Im}\omega \propto N/\ln N$ and $|z_\pm| - 1 \sim \ln N/N$ for large $N$. Such behavior of $z(N)$ leads to the different scaling for the edge-localized states with $N$. In the conventional case, the amplitude at the center of the structure is exponentially suppressed as compared to the one at the edge, $|\psi_{N/2}/\psi_1|^2 = \exp(-N/L_{\rm loc})$, where $L_{\rm loc}$ is the localization length, independent of $N$. Here, however, we find $|\psi_{N/2}/\psi_1|^2 \sim 1/N$. This is why we term the considered effect a mesoscopic NHSE. We note that this mesoscopic NHSE is qualitatively different from the critical NHSE [33,35–37], where $|\psi_{N/2}/\psi_1| = \text{const}(N)$.

*Mesoscopic versus conventional NHSE.* We now consider nonzero propagation losses in the waveguide. This means setting $\operatorname{Im}\varphi > 0$ in Eq. (1) so that the coupling $\propto \exp(i\varphi|m - n|)$ becomes finite ranged. Then the PBC spectrum $\omega(K)$ in Eq. (2) becomes complex valued with a nonzero point-gap winding number for $\chi \neq 0$ [23,24], enabling conventional NHSE. Figure 3 describes how the OBC eigenstates depend on $\operatorname{Im}\varphi$ and $N$. The color in Fig. 3(a) encodes the smallest eigenvalue for the brightest state $|z_1| - 1 = \min(|z_+|, |z_-|) - 1$. The blue color corresponds to mesoscopic NHSE ($|z_1| < 1$, and $|z_2| > 1$), and the red color corresponds to conventional NHSE, where $|z_1| > 1$, and $|z_2| > 1$. Figures 3(b) and 3(c) show the spatial profile of the brightest state for the two representative cases of mesoscopic and conventional NHSE, indicated in Fig. 3(a) by a circle and a diamond. It is clearly seen that for the conventional NHSE the localization is much stronger. Moreover, for the mesoscopic case, there exist two components of the eigenstate, localized at the left and right edges, although localization at the right edge is much more obvious. These components are depicted by red and blue lines in Fig. 3(c), and were calculated from Eq. (4). The insets in

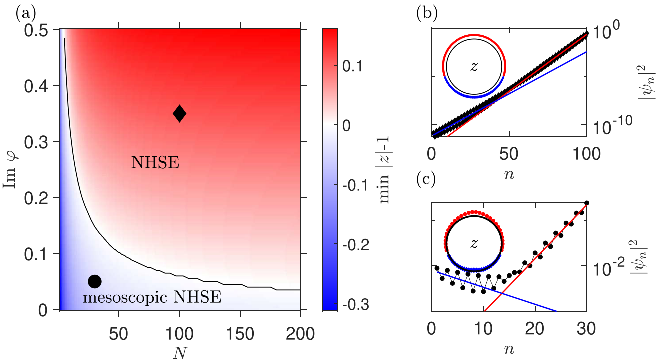

FIG. 3. (a) Minimal value of $|z(\omega)|$ depending on the number of emitter $N$ and loss $\operatorname{Im}\varphi$. The thin black line shows the boundary between mesoscopic and ordinary NHSE at $\min|z| = 1$. Two characteristic points $\{N, \operatorname{Im}\varphi\} = \{30, 0.05\}, \{100, 0.35\}$ are indicated by solid symbols. (b), (c) Symbols show wave functions $|\psi_n|^2$ of the states with largest $-\operatorname{Im}\omega$ for two characteristic parameters in (a). The red and blue lines show the two components of wave functions $\propto|z_1|^{2n}$ and $\propto|z_2|^{2n}$, found from Eq. (4). The insets in (b) and (c) show by red circles and blue diamonds the eigenvalues $z_{2,1} = \exp(iK_{2,1})$ for the OBC spectrum in the complex $z$ plane. The black circles correspond to the Brillouin zone boundary, $|z| = 1$. Other calculation parameters are $\operatorname{Re}\varphi = \pi/2$ and $\xi = 0.5$.

Figs. 3(b) and 3(c) show the complex values of $z_{1,2}$ for all the eigenstates. In the conventional NHSE, the values of $z_{1,2}$ with $|z_1| = |z_2|$ form the generalized Brillouin zone (GBZ) [4,38] that lies outside the unit circle, $|z| = 1$ [see Fig. 3(b)]. On the other hand, for the mesoscopic NHSE, one has $|z_1| < 1$ and $|z_2| > 1$.

*Regularization of the PBC.* Our central result is the link between the observed mesoscopic NHSE and the analytical properties of the PBC spectrum $\omega(K)$ in Eq. (2). We start by noting that the $N \to \infty$ limit of infinite structure with purely zero loss is not well defined. Even in vacuum, the photon propagator $1/[(\omega/c)^2 - K^2]$ has two poles at $K = \pm\omega/c$ that have to be carefully treated. There are two similar prescriptions, either deforming the integration path $\mathcal{C}$ in the complex $K$ plane or adding infinitesimal losses, that lead to the same result: The integral is determined by just one pole, corresponding to either the retarded or advanced Green's function [39]. Here, the dispersion law Eq. (2) has poles at the reservoir eigenmodes, $K = \pm\varphi$. Building on the same idea, we rigorously prove in the Supplemental Material [31] that if the contour $\mathcal{C}$ in the complex plane of $z = \exp(iK)$ satisfies the two conditions: (i) It surrounds only one of the poles and (ii) it is inversion symmetric, that is, $\forall z \in \mathcal{C}$ also $1/z \in \mathcal{C}$ (or, equivalently, $\forall K \in \log\mathcal{C}$ also $-K \in \log\mathcal{C}$), the image of this contour in the frequency plane $\omega(\mathcal{C})$ has a nonzero point-gap winding number around a certain reference energy $\varepsilon$ only for a chiral structure. In particular, the eigenmodes which decay in time (which have $\operatorname{Im}\omega < 0$) correspond to the contour surrounding the pole at $\exp(i\varphi)$ (see Supplemental Figs. S8 and S9 [31]). Our proof essentially generalizes the theorem in Ref. [38] for the waveguide-mediated coupling case. This is needed because Eq. (2) has different analytical properties compared to the tight-binding case. It is also relevant because of the recent interest in expanding the non-Hermitian skin effect to models beyond tight binding [43–45]. The winding number of $\omega(\mathcal{C}) - \varepsilon$ acts as a point-gap topological index. One of the possible ways to construct $\mathcal{C}$ is to consider points $\exp(iK) \in \mathcal{C}$ with complex $K$ defined by

$$K = \operatorname{Re}K - i\delta K(N)\sin\operatorname{Re}K, \quad -\pi \leqslant \operatorname{Re}K < \pi. \tag{7}$$

for the dispersion law Eq. (2). This is illustrated by the insets in Figs. 1(d) and 2(d). Note that the contour for $K$ goes below one pole at $K = +\varphi$ and above another pole at $K = -\varphi$. This means that the contour $\mathcal{C} = \exp(iK)$ will encircle only the pole at $\exp(i\varphi)$. For each $N$ we can choose $\delta K(N)$ and obtain $\mathcal{C}$ with $\omega(\mathcal{C})$ encircling the OBC spectrum (in the chiral case) or with a zero winding number (in the nonchiral case). The $\omega(\mathcal{C})$ contour is exactly the horseshoelike regularized PBCs shown in Figs. 1(a), 2(b), and 2(d). The gradient line color encodes the value of $\operatorname{Re}K$. For vanishing chirality, when $\omega(K) = \omega(-K)$, the horseshoe shrinks to a line with zero area and for larger chirality it expands to a full circle [Fig. 2(d)]. The curves in Figs. 1(d) and 2 have been calculated for $\delta K = 4/N$. A more precise scaling is $\delta K \propto \ln N/N$, which reflects the dependence of the $z$ values on $N$, $|z| - 1 \propto \ln N/N$. We stress that the winding number does not depend on $\delta K$ or on the particular choice of the regularization, even though the regularization parameter $\delta K$ in Eq. (7) to get $\omega(\mathcal{C})$ around the OBC is not universal. This is because the regularized PBC probes a deeper fundamental aspect, which is how the modes sit on the complex Riemann surface of $\omega(K)$. It is shown in Fig. 4 together with the OBC energy spectrum and the regularization path Eq. (7). The color of the Riemann surface encodes the value of $\operatorname{Re}K$. A clear distinction from the conventional NHSE is that the Riemann surface consists of the two leaves with the opposite signs of $\operatorname{Im}K$, corresponding to $|z_+| > 1$ and $|z_-| < 1$.

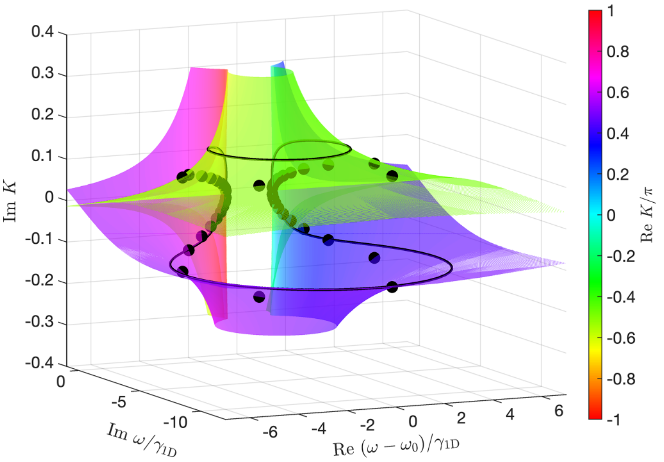

FIG. 4. Riemann surface of the dispersion law $\omega(K)$. Color encodes $\operatorname{Re}K$. Dots show the values of $K_\pm$ for the eigenfrequencies of the finite structure $\omega$. The thick black line corresponds to the contour $K = \operatorname{Re}K - i0.13\pi\sin\operatorname{Re}K$. Calculation has been performed for $\xi = 0.5$, $\varphi = \pi/2$, and $N = 20$.

*Summary.* The summary of our results is sketched in Table I. We distinguish between chiral and nonchiral structures and also between the structures with and without internal loss in the reservoir ($\operatorname{Im}\varphi = 0$ and $\operatorname{Im}\varphi > 0$). The latter are conventional non-Hermitian structures. They have a well-defined GBZ in the $z$ plane, and the loop in the image of the Brillouin zone $\omega$(BZ) is a signature of NHSE. For structures without internal loss, the distinction is more subtle. Naive PBC consideration predicts that the GBZ coincides with the Brillouin zone and $\omega(\text{BZ}) - \varepsilon$ has zero winding independent of chirality. The spectrum of eigenvalues (dotted magenta line in Table I) depends on the structure size and is not described

TABLE I. Schematic summary of the results for the complex spectra in $z = \exp[iK(\omega)]$ and $\omega$ planes. The thin black circles in the $z$ plane correspond to the BZ, $|z| = 1$, and the thick red circle to the GBZ. The dotted magenta line corresponds to OBC eigenstates, and green and cyan lines illustrate the contour $\mathcal{C} = \{\mathcal{C}_1, \mathcal{C}_2\}$ and its image $\omega(\mathcal{C})$.

| | no internal loss | | with internal loss |
|---|---|---|---|
| | naive PBC | size-dependent OBC | |
| Nonchiral | 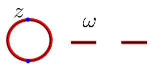 | 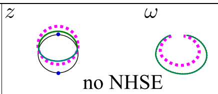 <br>no NHSE | 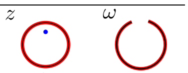 <br>no NHSE |
| Chiral | | 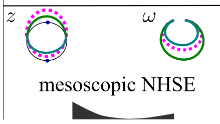 <br>mesoscopic NHSE | 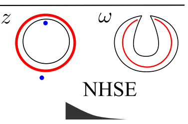 <br>NHSE |

by the conventional GBZ. However, the winding number of the regularized contour $\mathcal{C} = \{\mathcal{C}_1, \mathcal{C}_2\}$ image $\omega(\mathcal{C})$ still acts as a signature of a mesoscopic NHSE.

*Outlook*. Our results are not restricted to the waveguide quantum electrodynamics platform but apply to a broader class of non-Hermitian periodic systems. Namely, we find that the mesoscopic NHSE is present even for a relatively weak non-Hermiticity when the losses (or gain) are present only at the edges and not in the bulk. Formally, we mean here by weak non-Hermiticity that $\operatorname{rank}(H - H^\dagger) \ll \operatorname{rank}(H + H^\dagger)$. For example, for the Hamiltonian Eq. (1) $\operatorname{rank}(H - H^\dagger) = 2$, corresponding to the two loss channels [46]. In the Supplemental Material [31] we present two tight-binding models with edge losses, also exhibiting mesoscopic NHSE. The first model describes an array chirally coupled to a one-dimensional infinite lattice (playing the role of waveguide) and the second model describes a lossless array of sites with nearest-neighbor coupling linked to the lossy reservoirs at the edges (see also Refs. [34,35] considering localized non-Hermitian impurity). In the second model, the system is reciprocal and hence does not exhibit nontrivial point-gap topology even after regularization. Thus, the origin of the mesoscopic NHSE there may differ from the WQED case and requires further investigation. We can also expect mesoscopic NHSE beyond one-dimensional models, for example, in chiral all-dielectric metasurfaces [47,48].

*Acknowledgments*. The work of A.N.P. has been supported by research grants from the Center for New Scientists and from the Center for Scientific Excellence at the Weizmann Institute of Science. S.F. acknowledges a Simons Investigator in Physics grant from the Simons Foundation (Grant No. 827065)

---

[1] T. E. Lee, Anomalous edge state in a non-Hermitian lattice, Phys. Rev. Lett. **116**, 133903 (2016).

[2] V. M. Martinez Alvarez, J. E. Barrios Vargas, and L. E. F. Foa Torres, Non-Hermitian robust edge states in one dimension: Anomalous localization and eigenspace condensation at exceptional points, Phys. Rev. B **97**, 121401(R) (2018).

[3] F. K. Kunst, E. Edvardsson, J. C. Budich, and E. J. Bergholtz, Biorthogonal bulk-boundary correspondence in non-Hermitian systems, Phys. Rev. Lett. **121**, 026808 (2018).

[4] S. Yao and Z. Wang, Edge states and topological invariants of non-Hermitian systems, Phys. Rev. Lett. **121**, 086803 (2018).

[5] D. S. Borgnia, A. J. Kruchkov, and R.-J. Slager, Non-Hermitian boundary modes and topology, Phys. Rev. Lett. **124**, 056802 (2020).

[6] N. Okuma, K. Kawabata, K. Shiozaki, and M. Sato, Topological origin of non-Hermitian skin effects, Phys. Rev. Lett. **124**, 086801 (2020).

[7] E. J. Bergholtz, J. C. Budich, and F. K. Kunst, Exceptional topology of non-Hermitian systems, Rev. Mod. Phys. **93**, 015005 (2021).

[8] N. Hatano and D. R. Nelson, Vortex pinning and non-Hermitian quantum mechanics, Phys. Rev. B **56**, 8651 (1997).

[9] J. Zhong, K. Wang, Y. Park, V. Asadchy, C. C. Wojcik, A. Dutt, and S. Fan, Nontrivial point-gap topology and non-Hermitian skin effect in photonic crystals, Phys. Rev. B **104**, 125416 (2021).

[10] S. Longhi, Non-Hermitian skin effect beyond the tight-binding models, Phys. Rev. B **104**, 125109 (2021).

[11] K. Yokomizo, T. Yoda, and S. Murakami, Non-Hermitian waves in a continuous periodic model and application to photonic crystals, Phys. Rev. Res. **4**, 023089 (2022).

[12] K. Wang, A. Dutt, K. Y. Yang, C. C. Wojcik, J. Vučković, and S. Fan, Generating arbitrary topological windings of a non-Hermitian band, Science **371**, 1240 (2021).

[13] C. W. Hsu, B. Zhen, A. D. Stone, J. D. Joannopoulos, and M. Soljačić, Bound states in the continuum, Nat. Rev. Mater. **1**, 16048 (2016).

[14] P. Lodahl, S. Mahmoodian, S. Stobbe, A. Rauschenbeutel, P. Schneeweiss, J. Volz, H. Pichler, and P. Zoller, Chiral quantum optics, Nature (London) **541**, 473 (2017).

[15] A. S. Prasad, J. Hinney, S. Mahmoodian, K. Hammerer, S. Rind, P. Schneeweiss, A. S. Sørensen, J. Volz, and A. Rauschenbeutel, Correlating photons using the collective nonlinear response of atoms weakly coupled to an optical mode, Nat. Photonics **14**, 719 (2020).

[16] C. Liedl, S. Pucher, F. Tebbenjohanns, P. Schneeweiss, and A. Rauschenbeutel, Collective radiation of a cascaded quantum system: From timed Dicke states to inverted ensembles, Phys. Rev. Lett. **130**, 163602 (2023).

[17] L. Du, L. Guo, Y. Zhang, and A. F. Kockum, Giant emitters in a structured bath with non-Hermitian skin effect, Phys. Rev. Res. **5**, L042040 (2023).

[18] A. S. Sheremet, M. I. Petrov, I. V. Iorsh, A. V. Poshakinskiy, and A. N. Poddubny, Waveguide quantum electrodynamics: Collective radiance and photon-photon correlations, Rev. Mod. Phys. **95**, 015002 (2023).

[19] D. F. Kornovan, M. I. Petrov, and I. V. Iorsh, Transport and collective radiance in a basic quantum chiral optical model, Phys. Rev. B **96**, 115162 (2017).

[20] G. Fedorovich, D. Kornovan, A. Poddubny, and M. Petrov, Chirality-driven delocalization in disordered waveguide-coupled quantum arrays, Phys. Rev. A **106**, 043723 (2022).

[21] M. Yang, L. Wang, X. Wu, H. Xiao, D. Yu, L. Yuan, and X. Chen, Concentrated subradiant modes in a one-dimensional atomic array coupled with chiral waveguides, Phys. Rev. A **106**, 043717 (2022).

[22] Y.-C. Wang, J.-S. You, and H. H. Jen, A non-Hermitian optical atomic mirror, Nat. Commun. **13**, 4598 (2022).

[23] T. Yu and B. Zeng, Giant microwave sensitivity of a magnetic array by long-range chiral interaction driven skin effect, Phys. Rev. B **105**, L180401 (2022).

[24] B. Zeng and T. Yu, Radiation-free and non-Hermitian topology inertial defect states of on-chip magnons, Phys. Rev. Res. **5**, 013003 (2023).

[25] M. Voronov, E. Ivchenko, M. Erementchouk, L. Deych, and A. Lisyansky, Photoluminescence spectroscopy of one-dimensional resonant photonic crystals, J. Lumin. **125**, 112 (2007).

[26] K. L. Tsakmakidis, L. Shen, S. A. Schulz, X. Zheng, J. Upham, X. Deng, H. Altug, A. F. Vakakis, and R. W. Boyd, Breaking Lorentz reciprocity to overcome the time-bandwidth limit in physics and engineering, Science **356**, 1260 (2017).

[27] S. A. Mann, D. L. Sounas, and A. Alù, Nonreciprocal cavities and the time–bandwidth limit, Optica **6**, 104 (2019).

[28] K. L. Tsakmakidis, Y. You, T. Stefański, and L. Shen, Nonreciprocal cavities and the time-bandwidth limit: comment, Optica **7**, 1097 (2020).

[29] S. A. Mann, D. L. Sounas, and A. Alù, Nonreciprocal cavities and the time-bandwidth limit: reply, Optica **7**, 1102 (2020).

[30] S. Buddhiraju, Y. Shi, A. Song, C. Wojcik, M. Minkov, I. A. D. Williamson, A. Dutt, and S. Fan, Absence of unidirectionally propagating surface plasmon-polaritons at nonreciprocal metal-dielectric interfaces, Nat. Commun. **11**, 674 (2020).

[31] See Supplemental Material at http://link.aps.org/supplemental/10.1103/PhysRevA.109.L061501 for auxiliary results and details of derivations, which contains Refs. [40–42].

[32] C.-X. Guo, C.-H. Liu, X.-M. Zhao, Y. Liu, and S. Chen, Exact solution of non-Hermitian systems with generalized boundary conditions: Size-dependent boundary effect and fragility of the skin effect, Phys. Rev. Lett. **127**, 116801 (2021).

[33] L. Li, C. H. Lee, S. Mu, and J. Gong, Critical non-Hermitian skin effect, Nat. Commun. **11**, 5491 (2020).

[34] Y. Liu, Y. Zeng, L. Li, and S. Chen, Exact solution of the single impurity problem in nonreciprocal lattices: Impurity-induced size-dependent non-Hermitian skin effect, Phys. Rev. B **104**, 085401 (2021).

[35] B. Li, H.-R. Wang, F. Song, and Z. Wang, Scale-free localization and $\mathcal{PT}$-symmetry breaking from local non-Hermiticity, Phys. Rev. B **108**, L161409 (2023).

[36] K. Yokomizo and S. Murakami, Scaling rule for the critical non-Hermitian skin effect, Phys. Rev. B **104**, 165117 (2021).

[37] C.-X. Guo, X. Wang, H. Hu, and S. Chen, Accumulation of scale-free localized states induced by local non-Hermiticity, Phys. Rev. B **107**, 134121 (2023).

[38] K. Zhang, Z. Yang, and C. Fang, Correspondence between winding numbers and skin modes in non-Hermitian systems, Phys. Rev. Lett. **125**, 126402 (2020).

[39] V. B. Berestetskii, E. M. Lifshitz, and L. P. Pitaevskii, *Quantum Electrodynamics* (Butterworth-Heinemann, Oxford, UK, 1982), Vol. 4.

[40] F. Roccati, S. Lorenzo, G. Calajò, G. M. Palma, A. Carollo, and F. Ciccarello, Exotic interactions mediated by a non-Hermitian photonic bath, Optica **9**, 565 (2022).

[41] E. L. Ivchenko, A. I. Nesvizhskii, and S. Jorda, Bragg reflection of light from quantum-well structures, Phys. Solid State **36**, 1156 (1994).

[42] Y. Ke, A. V. Poshakinskiy, C. Lee, Y. S. Kivshar, and A. N. Poddubny, Inelastic scattering of photon pairs in qubit arrays with subradiant states, Phys. Rev. Lett. **123**, 253601 (2019).

[43] K. Yokomizo, T. Yoda, and Y. Ashida, Non-Bloch band theory of generalized eigenvalue problems, Phys. Rev. B **109**, 115115 (2024).

[44] H. Ding and K. Ding, Non-Bloch theory for spatiotemporal photonic crystals assisted by continuum effective medium, arXiv:2401.12536.

[45] Y.-M. Hu, Y.-Q. Huang, W.-T. Xue, and Z. Wang, Non-Bloch band theory for non-Hermitian continuum systems, arXiv:2310.08572.

[46] S. J. Masson, I. Ferrier-Barbut, L. A. Orozco, A. Browaeys, and A. Asenjo-Garcia, Many-body signatures of collective decay in atomic chains, Phys. Rev. Lett. **125**, 263601 (2020).

[47] Y. Kivshar, Mie scattering yields chiral nonlinearity, Nat. Photonics **16**, 89 (2022).

[48] K. Koshelev, Y. Tang, Z. Hu, I. I. Kravchenko, G. Li, and Y. Kivshar, Resonant chiral effects in nonlinear dielectric metasurfaces, ACS Photonics **10**, 298 (2023).